

In situ LA–ICP–MS dating of monazite from aluminous gneisses: insights on the tectono-metamorphic history of a granulite-facies domain in the central Grenville Province

Introduction

In recent years, in situ dating of monazite has become a key tool for unravelling complex metamorphic histories of high-grade terranes. Although less precise than the isotopic dilution – thermal ionization mass spectrometry (ID–TIMS) method, in situ techniques such as electron probe micro-analysis (EPMA) and laser ablation – inductively coupled plasma – mass spectrometry (LA–ICP–MS) have better spatial resolution, permitting dating of distinct zones in individual monazite grains as well as linking ages with specific microstructural settings (e.g., Simonetti et al. 2006; Kelsey et al. 2007, 2008; Cutts et al. 2010; Langone et al. 2011; Kelly et al. 2012; Gervais and Hynes 2012).

Recent studies have shown that the diffusivity of Pb in monazite is low, comparable to that of zircon (Cherniak et al. 2004), and it is increasingly accepted that even in high-grade metamorphic rocks monazite ages most likely represent growth events rather than resetting (e.g., Kelsey et al. 2008; Dunning and Indares 2010). During prograde metamorphism of aluminous rocks, monazite typically forms from upper greenschist throughout the amphibolite facies by reactions that involve not only other accessory phases but also rock-forming silicates. However, during anatexis under granulite-facies conditions, monazite is predicted to dissolve in the melt and to grow again only when melt crystallizes during cooling (Kelsey et al. 2008; Spear and Pyle 2010). In addition, monazite might also grow at sub-solidus conditions if there is fluid infiltration. Interpretation of in situ monazite ages is a complicated enterprise for many reasons. For instance, low precision of the U–Pb data limits the ability to distinguish monazite growth events occurring within a short period of time (e.g., a few tens of million years). Also, assigning monazite U–Pb ages to different parts of a metamorphic *P–T* (pressure–temperature) path(s) remains difficult, as internal elemental zoning, even if well documented (e.g., EPMA), cannot always be related to specific metamorphic reactions (e.g., Harrison et al. 2002; Spear and Pyle 2002; Williams et al. 2007; Kelsey et al. 2008). This is particularly challenging in the case of long-duration orogens, in which the middle to lower crust remains under high metamorphic temperatures over several tens of million years (large hot orogens; Beaumont et al. 2006).

The Grenville Province is a prime example of an ancient, long-duration (ca. 1100–980 Ma) large hot orogen, often compared to the Himalaya–Tibet system (e.g., Rivers 2008). Geological research during the last few decades has provided a clear image of the general orogenic architecture and metamorphic styles of the Province (cf., Rivers et al. 2012) and resulted in compelling first-order tectonic interpretations. For instance, it is established that during the culmination of the Grenvillian orogeny (ca. 1090–1050 Ma) large parts of the orogenic hinterland (high-*P* and mid-*P* segments or belts of Rivers et al. 2012) were subjected to granulite-facies metamorphism, and heterogeneous flow of this middle to lower orogenic crust is inferred to have

played a key role in the tectonic evolution of the Province (Jamieson et al. 2007, 2010; Jamieson and Beaumont 2011). In addition, the present juxtaposition of these high-grade metamorphic belts with crustal segments affected by a lower-grade (or imperceptible) Grenvillian overprint is attributed to orogenic collapse (ca. 1000–980 Ma; Rivers 2012). In contrast, the structurally lower Parautochthonous belt of the Province was metamorphosed during the presumed orogenic collapse, and final propagation of the orogen to the northwest (Rivers 2009).

Individual rocks from various parts of the granulite-facies segments show significant spread in metamorphic ages within the ca. 1090–1040 Ma interval (e.g., Slagstad et al. 2004; Dunning and Indares 2010), raising the possibility of multiple metamorphic pulses, or protracted residence under high-*T* conditions. In addition, parts of the hinterland in the central and eastern Grenville Province record a late Grenvillian thermal event (990–970 Ma), broadly coeval with the main metamorphism in the Parautochthonous belt. This event is manifested by pervasive intrusions of ultrapotassic dykes, inferred to have originated from metasomatized subcontinental lithosphere (Owens and Tomascak 2002; Valverde Cardenas et al. 2012), felsic pegmatites, and granite (Gower and Krogh 2002; Dunning and Indares 2010), but its effect on the country rocks has not been investigated.

The work presented here aims to reassess the spread of ID–TIMS monazite ages previously identified by Dunning and Indares (2010) in granulite-facies anatectic aluminous rocks from the Manicouagan area (central Grenville Province), and evaluate a potential contribution from the late Grenvillian thermal event. To that end, in situ LA–ICP–MS U–Pb dating of monazite was undertaken on the same samples as those of Dunning and Indares (2010), this time with the potential to place the age data in the context of the general microstructure of the rocks, as well as in the context of specific zones in single monazite grains. Metamorphic microstructures, and *P–T* paths inferred by phase equilibria modelling, are presented in another contribution (Lasalle and Indares 2014). Here the focus is on the monazite populations, their microstructural setting in thin section, and their U–Pb ages.

Geological background

Regional setting

This study focuses on the Manicouagan area in the central Grenville, enclosing the reservoir of the same name (Fig. 1; for a comprehensive geological overview, see Dunning and Indares 2010). In this area, the hinterland of the Province is located structurally above Archean to Paleoproterozoic rocks of the Parautochthonous Gagnon terrane (Rivers et al. 1989; Jordan et al. 2006; van Gool et al. 2008) and consists of lithotectonic domains made of 1.7–1.2 Ga Mesoproterozoic rocks, best exposed on the shoreline of the reservoir (Indares et al. 2000; Indares and Dunning 2004; Dunning and Indares 2010). During the culmination of the Grenvillian orogeny, the northern (Manicouagan Imbricate Zone; MIZ; Fig. 1) and

southern (Canyon and Island domains) portions of the hinterland were metamorphosed under high-*P* and mid-*P* granulite-facies conditions, respectively (Indares and Dunning 2001, 2004; Dunning and Indares 2010), whereas to the east, between these two, the Hart Jaune terrane displays no record of Grenvillian age high-grade metamorphism and belongs to the “orogenic lid” of Rivers (2008). In contrast, parautochthonous units on the western shore of the reservoir were metamorphosed under high-*P* granulite-facies conditions later, during the waning stages of the Grenvillian orogeny (Jordan et al. 2006).

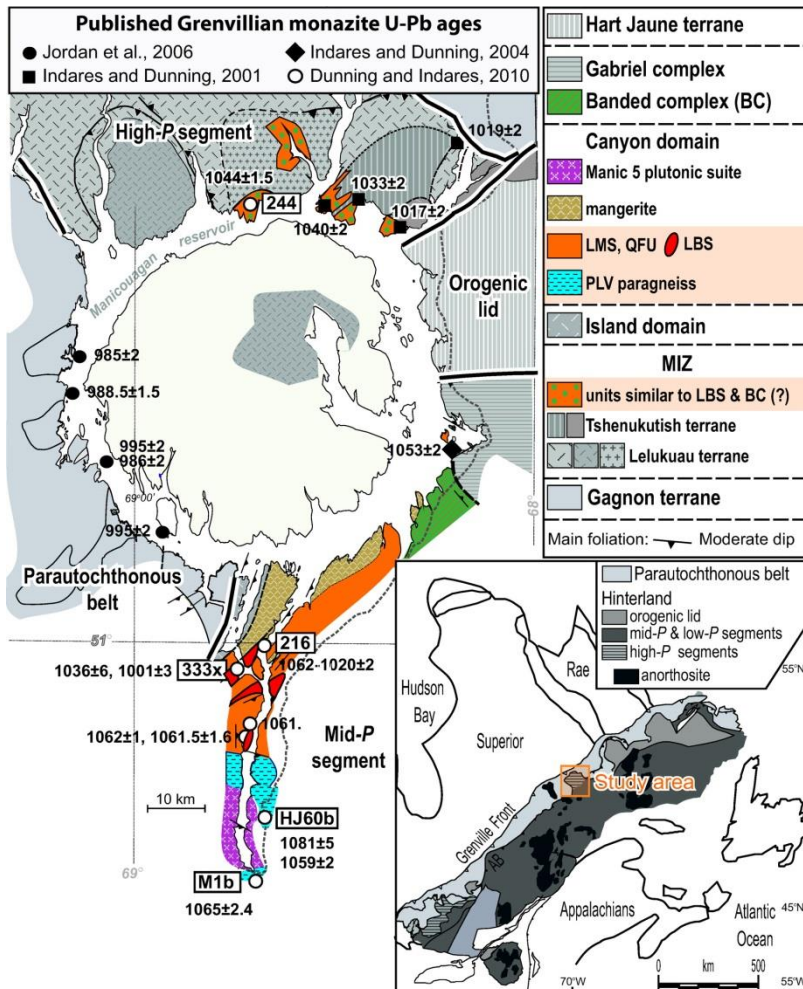


Fig. 1. Simplified geological map of the Manicouagan area (inspired by Indares and Moukhsil 2013) showing previously published Grenvillian U–Pb monazite data (ID–TIMS; Dunning and Indares 2010), and inset map showing the general framework and location of the Grenville Province. MIZ, Manicouagan Imbricate Zone; PLV, Complexe de la Plus Value; QFU, layered quartzofeldspathic unit; LMS, layered mafic suite; LBS, layered bimodal sequence. Ages in Ma. (Colour in online version.)

The samples of interest come mostly from the Canyon domain, which is exposed in the southern part of the Manicouagan reservoir (Fig. 1). This domain is mainly composed of layered units, first documented by Dunning and Indares (2010) and further characterized by Indares and Moukhsil (2013). A ca. 1.5 Ga paragneissic sequence, known as the Complexe de la Plus Value (PLV; first defined farther east by Moukhsil et al. 2012), is exposed in the southern part of the domain. In contrast, the central and northern parts are dominated by a complex lithologic association, including a ca. 1.4 Ga old layered mafic suite (LMS), interleaved with a layered quartzofeldspathic unit (QFU) of unknown age, and a ca. 1.24 Ga layered bimodal

mafic–felsic sequence (LBS). The LBS is inferred to represent remnants of a volcanic belt emplaced in an extensional setting, and locally contains aluminous layers, some of which are attributed to pre-metamorphic hydrothermal alteration of felsic volcanic rocks (Indares and Moukhsil 2013; Lasalle et al. 2013; Hindemith 2014). Rocks typical of the LBS are also recognized 50 km to the north, in the southern tip of the Manicouagan Imbricate Zone, in the high-*P* segment (MIZ; Fig. 1). In addition, the southern part of the Canyon domain is pervasively injected by late to post-tectonic ultrapotassic dykes and felsic pegmatite that were dated at 980 ± 3 and 995 ± 3.5 Ma, respectively (Dunning and Indares 2010).

Summary of metamorphic ages in the Manicouagan area

Available age constraints for the Grenvillian metamorphism include monazite (Fig. 1), zircon and titanite data. In the Canyon domain, U–Pb monazite (ID–TIMS) ages of single grains from anatectic aluminous rocks range between ca. 1081 and 1020 Ma, with a varied spread within individual samples, and the largest concentration at ca. 1062–1059 Ma (Dunning and Indares 2010). In addition, recent metamorphic zircon U–Pb data (in situ LA–ICP–MS; Lasalle et al. 2013) for similar rocks yielded Grenvillian ages between ca. 1076 and 1044 Ma.

Grenvillian monazite ID–TIMS ages from other parts of the Manicouagan area (Fig. 1) include ca. 1050 Ma in the mid-*P* Gabriel complex (Indares and Dunning 2004), ca. 1044–1033 Ma in the high-*P* Manicouagan Imbricate Zone (Indares and Dunning 2001; Dunning and Indares 2010), with ca. 1020 Ma at the structural top, near the boundary with the Hart Jaune terrane, and 995–985 Ma in the Gagnon terrane (Jordan et al. 2006). Finally, titanite ages from the Canyon domain and the Manicouagan Imbricate Zone range between ca. 1000 and 985 Ma (Cox et al. 1998; Dunning and Indares 2010).

So far, these data suggest the following: (i) the monazite ages from individual samples are more clustered in the high-*P* segment relative to the mid-*P* segment; (ii) the latter also shows older ages (e.g., at 1080 and 1060 Ma) which are absent from the high-*P* segment; and (iii) high-grade metamorphism in the Gagnon terrane is distinctly younger than in any part of the hinterland of the Manicouagan area.

The previous studies also revealed some pre-Grenvillian ages from inherited monazite (ID–TIMS; Fig. 1): ca. 1740–1720 Ma in the Gagnon terrane (Jordan et al. 2006); ca. 1478–1467 Ma in the Gabriel complex (Indares and Dunning 2004) and the Canyon domain (Dunning and Indares 2010); and ca. 1220 Ma from the high-*P* portion of the LBS (intercept age, Dunning and Indares 2010). In addition, the zircon study by Lasalle et al. (2013) identified pre-Grenvillian metamorphic events in the PLV in Canyon domain at about 1.4 and 1.2 Ga, which are probably linked to the emplacement of the LMS and LBS into their country rocks.

Sample locations

Five samples were selected for in situ monazite dating using LA–ICP–MS: one from an aluminous paragneiss of the PLV (sample HJ60b) and four from aluminous layers of the LBS (samples 244, 216a, 216c,

and 333x; [Fig. 1](#)). Among the latter, sample 244 is inferred to be of metasedimentary origin, whereas the rest are inferred to be derived from hydrothermally altered felsic volcanic rocks ([Lasalle et al. 2013](#)). The rocks are from the Canyon domain (mid-*P* portion of the hinterland) except for sample 244, which was collected on the extension of LBS into the high-*P* segment. Sample 333x is the same one used for the previous ID-TIMS study while samples 216a, 216c, HJ60b, and 244 are different samples from the same outcrops and rock types previously analyzed.

Summary of the petrography and *P*–*T* data

The detailed petrography of the rock samples is discussed in Lasalle and Indares (2014); therefore, only a brief summary is presented here. All rocks are anatectic aluminous gneisses with the main mineral assemblage of quartz–K-feldspar–plagioclase–garnet–Al-silicate–biotite and leucosome, with trace amounts of rutile and (or) ilmenite. Al-silicate is sillimanite in the mid-*P* samples (samples HJ50b, 216a, 216c, 331x), and kyanite in the high-*P* sample 244.

The general distribution of phases in polished thin sections is shown in [Fig. 2](#) by means of false-colour maps (see also Lasalle and Indares 2014). The metasedimentary samples 244 and HJ60b have the highest proportions of garnet + biotite + Al-silicate and mainly consist of large garnet porphyroblasts, variably overgrowing Al-silicate, and domains rich in Al-silicate + biotite, enclosed in a quartzofeldspathic matrix (Figs. 2a, 2b). In the samples inferred to have acquired their aluminous character by hydrothermal alteration of felsic rocks (samples 216a, 216c, and 333x), garnet + biotite + sillimanite is concentrated in thin seams, locally mantled by plagioclase (sample 216a) or overgrown by variably elongated garnet, and scarce biotite is mainly associated with garnet and sillimanite. Samples 216a and 216c display a layered quartzofeldspathic matrix with small and evenly distributed garnets (sample 216c; [Fig. 2d](#)), and a wider range of garnet sizes in sample 216a ([Fig. 2c](#)). Sample 333x is characterized by a K-feldspar dominated matrix enclosing elongated quartz domains and aggregates of framboidal garnet which define a large discontinuous lens ([Fig. 2e](#)).

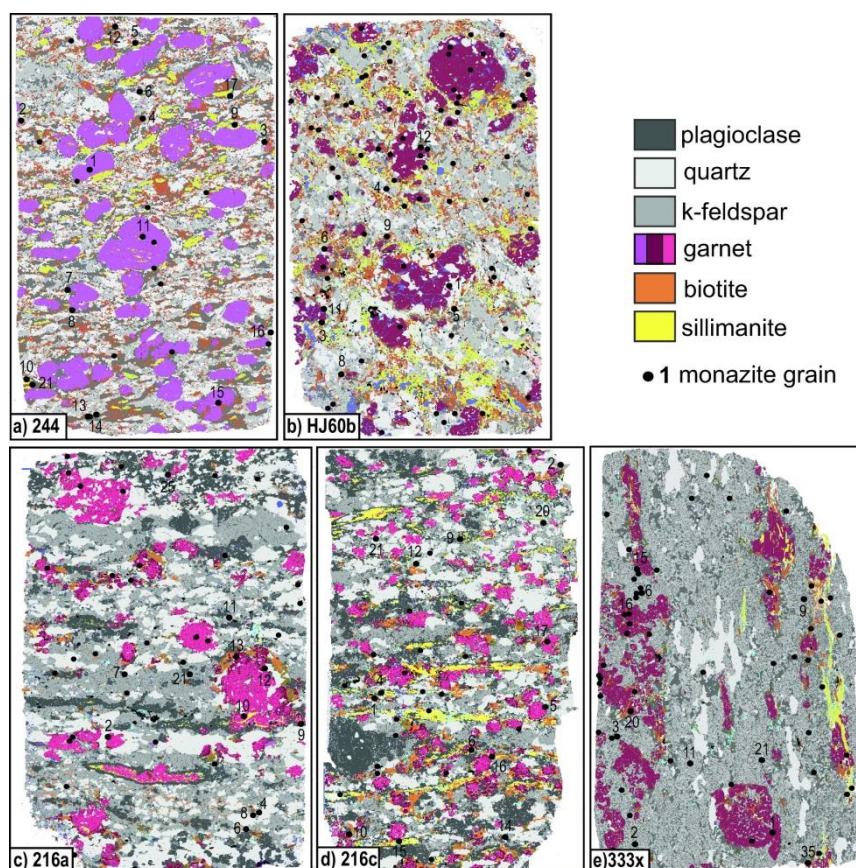


Fig. 2. False-colour scanning electron microscope – Mineral Liberation Analysis (SEM-MLA) maps of polished thin sections, samples (a) 244, (b) HJ60b, (c) 216a, (d) 216c, and (e) 333x, highlighting the main mineralogy, texture, and locations of monazite (black dots) for each sample (modified after Lasalle and Indares 2014). Numbers were added for the monazite grains that are discussed in the text, tables, and other figures.

At a finer scale, all samples display films and (or) optically continuous pools of feldspar engulfing resorbed quartz, biotite, and (or) Al-silicate. These microstructures are mostly observed as composite inclusions in garnet, but also, more rarely, in the matrix and are inferred to represent former melt pseudomorphs (Lasalle and Indares 2014).

The peak metamorphic mineral assemblage, in conjunction with microstructural evidence of garnet overgrowing Al-silicate and the presence of former anatectic melt, is consistent with P – T conditions within the field of the continuous biotite-consuming fluid-absent melting reaction $\text{Al-silicate} + \text{biotite} + \text{quartz} + \text{plagioclase} \rightarrow \text{garnet} + \text{K-feldspar} + \text{liquid}$. In all samples, garnet is variably corroded by biotite (\pm sillimanite in the mid- P samples), consistent with back-reaction during the subsequent melt crystallization. However, overall good preservation of the peak assemblage suggests that part of the melt may have escaped from its source rocks, a feature commonly observed in rocks undergoing anatexis in orogenic environments (e.g., Brown 2004).

Metamorphic microstructures and mineral chemistry data integrated with phase equilibria modelling suggest the following: (i) a steep prograde P – T path up to ~ 14.5 kbar (1 kbar = 100 MPa) and 890 °C, followed by decompression with minor cooling to the solidus at ~ 11 kbar and 870 °C (just above the kyanite–sillimanite

transition) in the high-*P* sample 244, similar to those inferred in other parts of the Manicouagan Imbricate Zone; and (ii) *P*–*T* paths with moderate dP/dT gradients, confined below the sillimanite–kyanite transition, with maximum *P*–*T* at ~9.5 kbar and 850 °C, and a retrograde portion to ~8 kbar and 820 °C in the case of sample HJ60b (Lasalle and Indares 2014).

In addition, the mid-*P* aluminous rocks from both the PLV and the LBS display local subtle microstructures consistent with greenschist metamorphic overprint. These include fractured garnet, with the cracks filled by chlorite (e.g., samples HJ60b, 216; Figs. 3a, 3b), sillimanite pseudomorphed by a fine-grained mixture of an unidentified phase, probably sericite (sample HJ60b; Fig. 3c), and graphite rimmed by sericite aggregates (Fig. 3d).

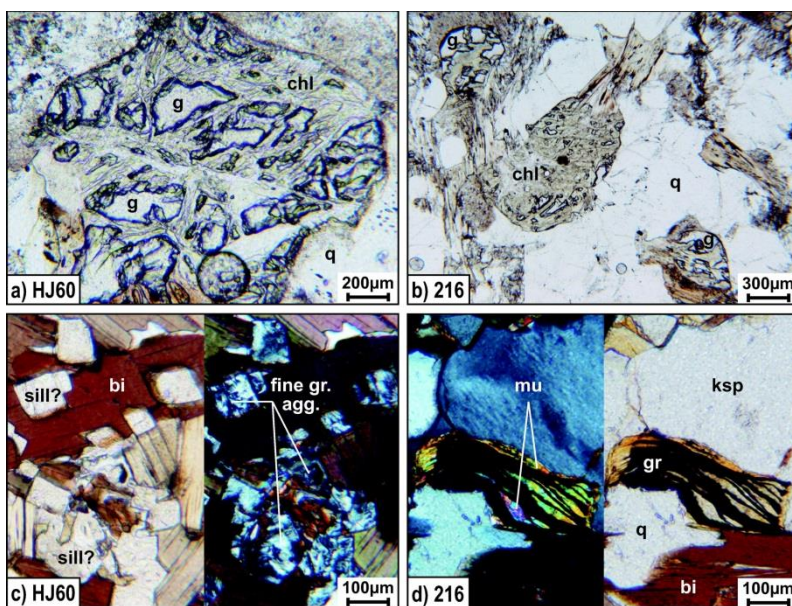


Fig. 3. Photomicrographs illustrating the late greenschist (?) metamorphic features present in samples HJ60b and 216, viewed in PPL (plane-polarized light) and XPL (crossed-polarized light): (a) garnet porphyroblast replaced by chlorite (sample HJ60; PPL); (b) “cracked eggs” garnet, replaced by chlorite (sample 216a; PPL); (c) sillimanite pseudomorphed by fine aggregates of sericite (?) (sample HJ60; PPL and XPL); (d) graphite rimmed by muscovite (sample 216; XPL and PPL). bi, biotite; chl, chlorite; fine gr. agg., fine-grained aggregates; g, garnet; gr, graphite; ksp, k-feldspar; mu, muscovite; q, quartz; sill, sillimanite.

Description of the monazite populations

Imaging techniques

In each polished thin section, monazite (cf., dark dots Fig. 2) was identified by SEM–MLA mineral mapping (Lasalle and Indares 2014). The maps were produced by a Mineral Liberation Analysis (MLA) software (developed by JKTech, University of Queensland, Australia) linked to a FEI Quanta 400 environmental scanning electron microscope (SEM) at the Bruneau Center of Memorial University. The SEM was set up with an accelerating voltage of 25 kV, a beam current of 10 nA, a 2 mm frame size (or horizontal field width), a dwell time of 10 ms, and a step size of 50 μm. The MLA software was used to generate a point-

counted estimation of mineral proportions and a composition-sensitive false-colour map of the mineral associations and textural relationships (Shaffer et al. 2008; Shaffer 2009). In addition, a first-order determination in terms of Th contents and zoning was done with the SEM. To map each monazite grain in more detail, the thin sections had to be mapped a second time, with the SEM coupled to the energy dispersive X-ray (EDX) and MLA software. Using the same SEM parameters (e.g., contrast/brightness settings) used for the full-section mapping, we set up the scan to exclude all minerals darker than the 8 bit brightness value of 130, which appeared to have excluded Fe oxides, but included minerals as bright or brighter than pyrrhotite, thus the presence of some grains of zircon and apatite with the monazite. Figure 4 presents each monazite grain in a unique way which highlights the general variations within and between samples. The largest grains selected for dating were also imaged in backscatter electron (BSE) imaging (Fig. 5). In addition, some grains with the most complex internal texture (grains 1–4 and 20 from sample 216c) were mapped for Th, U, Pb, and Y (Fig. 6) using a JEOL 8200 Electron microprobe, equipped with five wavelength spectrometers, at Dalhousie University. The voltage was set to 15 kV and the probe current between 0.10^{-7} and 0.10^{-8} A.

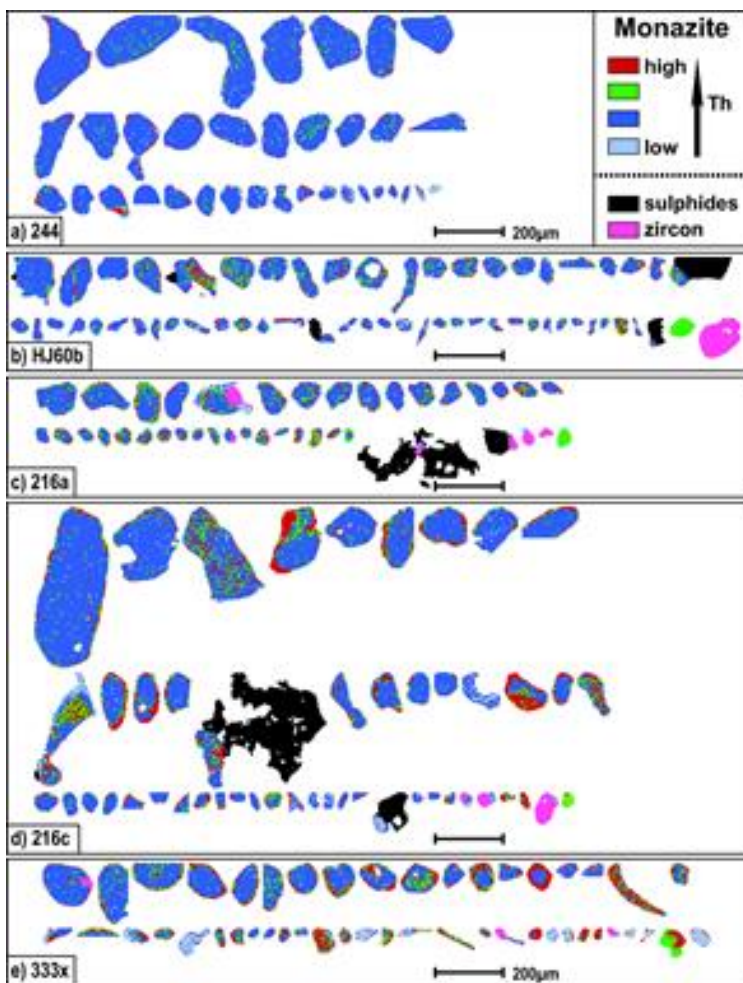


Fig. 4. Silhouettes of monazite grains showing Th zoning and associated minerals, obtained by SEM mapping: (a) sample 244; (b) sample HJ60b; (c) sample 216a; (d) sample 216c; (e) sample 333x.

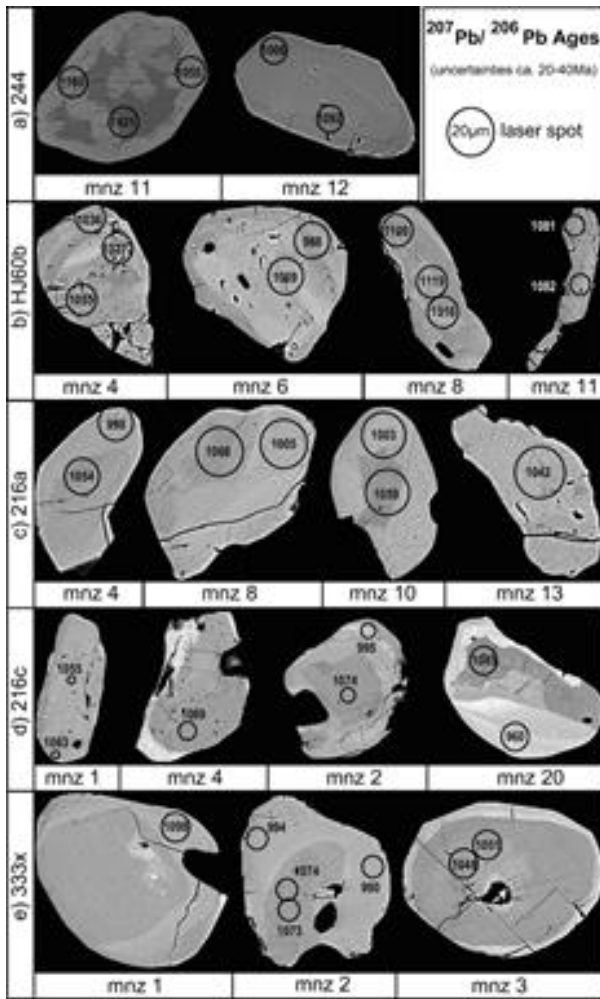


Fig. 5. Monazite (mnz) zoning as seen on BSE images, and location of the LA–ICP–MS spot analyses (20 μm) labelled with the corresponding $^{207}\text{Pb}/^{206}\text{Pb}$ age: (a) sample 244; (b) sample HJ60b; (c) sample 216a; (d) sample 216c; (e) sample 333x. These grains are the most characteristic ones in terms of internal BSE zoning and (or) U–Pb ages.

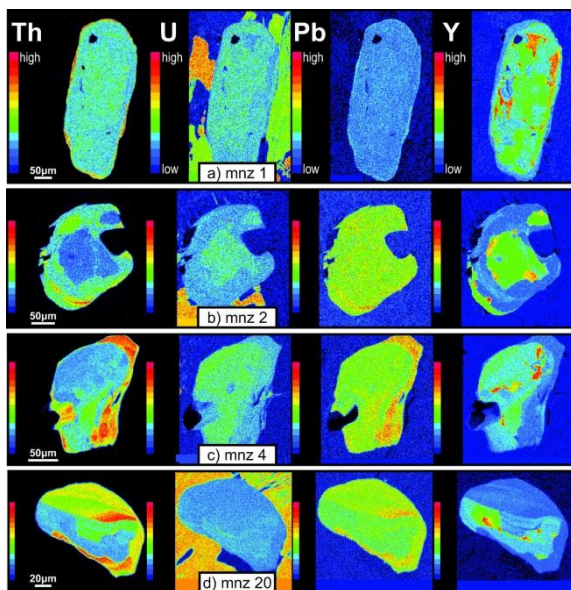


Fig. 6. Examples of qualitative chemical maps, acquired by EPMA, of five monazite grains from section 216c that display the most characteristic internal zoning in Th, U, Pb, and Y: (a) grain 1; (b) grain 2; (c) grain 4; (d) grain 20.

Microstructural setting and main characteristics of monazite

All samples contain abundant monazite, mostly in the matrix (Fig. 2). Monazite is rare in garnet cores but it is commonly located at garnet rims, or in their vicinity (Fig. 2), and within biotite corroding garnet (e.g., grains 12 and 13 in sample 216a; Fig. 2c). Matrix monazite is often found in a 500 μm radius around garnet, and in sample 333x it is mainly concentrated in domains with seams of sillimanite overgrown by garnet and framboidal garnet aggregates. Monazite in the matrix occurs isolated, or more rarely, in loose clusters (grains 13, 14 in sample 244; Fig. 2a; and grains 4, 8 in sample 216a; Fig. 2c), and a few grains in all samples but sample 244 are attached to, or overgrow, zircon (Figs. 4b–4e).

The number of monazite grains per thin-section ranges between 33 (sample 244) and 54 (sample HJ60b). The largest grains (≥ 200 μm in length) occur in samples 244 and 216c, whereas maximum sizes are generally up to 150 μm elsewhere (Fig. 4), and the smallest grains are ≤ 50 μm in all samples. In addition, Fig. 4 shows the first-order zoning in Th. In the majority of cases, individual grains are homogeneous, with relatively low Th contents or show rims variably enriched in Th. In addition, a few grains (in all samples but sample 244) have patchy zones variably enriched in Th, and Th-depleted rims. Most homogeneous are the monazite grains of sample 244, in which Th-enriched rims are ≤ 5 μm and discontinuous, whereas those of sample 216c show the largest variety of patterns, hence the additional imaging of a few of the most representative grains with EPMA (Fig. 6).

Grain 1 is an example of monazite with a very thin (< 5 μm) and discontinuous Th-enriched rim around a large and homogeneous core depleted in Th and Pb, and a complex patchy zoning in Y which clearly stops before the rim outline (Fig. 6a). Monazite 2 displays the most complex zoning in EPMA (Fig. 6b). A 50 μm thick composite rim is defined by relatively higher Th content. In contrast, Th concentration is relatively lower in two places, matching areas of relatively higher Y concentration; the main core at the center of the grain of ~ 150 μm in diameter and a significantly smaller (30–40 μm) rounded domain first identified as rim. This feature could represent the relict core of a second monazite which was overgrown by the thick rim. In grains 4 and 20 (Fig. 6c, 6d) the Th-enriched overgrowth is also discontinuous but significantly thicker (up to ~ 20 μm). The core has relatively low U, with some enriched distinct domains (mnz 20) or diffuse patches (mnz 4) in its center. In all four grains, zoning in Pb concentration matches that of Th, with relative enrichment at the rim while small high Y patches are again limited to the core area (Fig. 6).

Monazite U–Pb dating by LA–ICP–MS

Analytical method

The LA–ICP–MS analyses were carried out directly on monazite grains in thin sections, using the Finnigan Element XR2 instrument at Memorial University (Bruneau Center, MAF-IIC 2 lab). The 2.5 cm \times 5 cm thin sections were cut in half and analyzed over 3 days divided into 13 analytical runs. Each half thin section was placed at the center of the cell, in a custom-made holder which also holds one small 5 mm epoxy mount containing the Trebilcock monazite standard (TIMS age 272 Ma, Tomascak et al. 1996) used as the reference

material, and about a dozen grains of monazite KMO3-72 used as the secondary standard (TIMS age 1822 ± 1.5 Ma, G. Dunning, unpublished data). Reducing the thin-section size and centering it in the sample holder and ablation cell was done to minimize discrepancies between data collected on grains which would have been at the far corners of the section, and data from grains closer to the center. Such biases are noted in other studies and are suggested to be due to differences in flow circulation within the cell (Fisher et al. 2011). For each sample, up to 20 large monazite grains were analyzed (cf. Fig. 4), using a spot diameter of $20 \mu\text{m}$ and following the standard bracketing technique. Each of the 13 analytical runs comprised between ~ 30 and 70 analyses (including that of the reference material and secondary standard). Trebilcock monazite was analyzed three or four times at the beginning and end of each run, and once every two or three analyses of unknowns. The secondary standard KMO3-72 was analyzed regularly at least four times per run. A single analysis was <2 min long, including ~ 30 s of gas blank, ~ 50 s ablation, and ~ 20 s of washout. The instrument tuning parameters were slightly refined between the first and fifth run of day 1, varying between 2–3 J and 2–4 Hz. After that, the combination 2 J – 2 Hz was kept constant during the remaining eight runs. A list of the detailed instrument settings is presented Table 1. The freeware Iolite software (Paton et al. 2010) running in IgorPro (WaveMetrics, Inc; www.wavemetrics.com) was used for the data reduction; down-hole fractionation was corrected with a “smoothed cubic spline” model and the instrumental drift with the “automatic” type of spline. Once processed with Iolite, the data were exported in EXCEL, and Isoplot (version 3.34; Ludwig 2003) was used to calculate weighted average ages and make Tera-Wasserburg plots.

Table 1. Operating conditions and instrument settings used for the U–Pb LA–ICP–MS analyses.

Operating conditions	Instrument setting
ICP–MS	
Type	High-resolution double-focusing magnetic sector
Brand and model	Thermo Finnigan Element XR
Forward power	1349 W
Gas flows (L/min)	
Cool (Ar)	16
Auxiliary (Ar)	1.01–1.02
Sample (Ar)	0.875
Carrier (He)	1.080
Laser	
Type of laser	ArF excimer
Brand and model	GEOLAS 193 nm excimer
Laser wavelength	193 nm
Pulse width	20 ns
Spot size	20 μm
Repetition rate	2–4 Hz
Laser fluence	2–3 J/cm ²
Data acquisition parameters	
Resolution mode	Low
Data acquisition protocol	Time-resolved analysis
Scan mode	E-scan
Scanned masses	204, 206–208, 232, 238
Settling time	0.001 s, 0.030 s (for 204)
Sample time	0.01 s, 0.02 s (for 206), 0.03 s (for 207)
Samples per peak	10
Number of scans	975
Detector mode	Counting; analog for 238
Detector dead time	19 ns
Background collection	30 s
Ablation duration	50 s
Washout	20–40 s
Standardization and data reduction	
External standard used	KMO3-72
Reference standard used	Trebilcock
Data reduction software used	Iolite

Expected precision and accuracy based on standard data

The monazite standard Trebilcock was analyzed 235 times in total, and 39 outlier analyses (17%) were discarded (Fig. 7). The outliers were identified on the basis of their *measured* U/Pb ratios. If one or more ratios were $\geq 2\%$ away from the mean calculated for the full run, the analysis was discarded. The weighted average $^{206}\text{Pb}/^{238}\text{U}$ age calculated for Trebilcock at 272.0 ± 0.41 Ma (mean square weighted deviation (MSWD) = 0.63) agrees with the TIMS data at 272 ± 2 Ma (Tomascak et al. 1996).

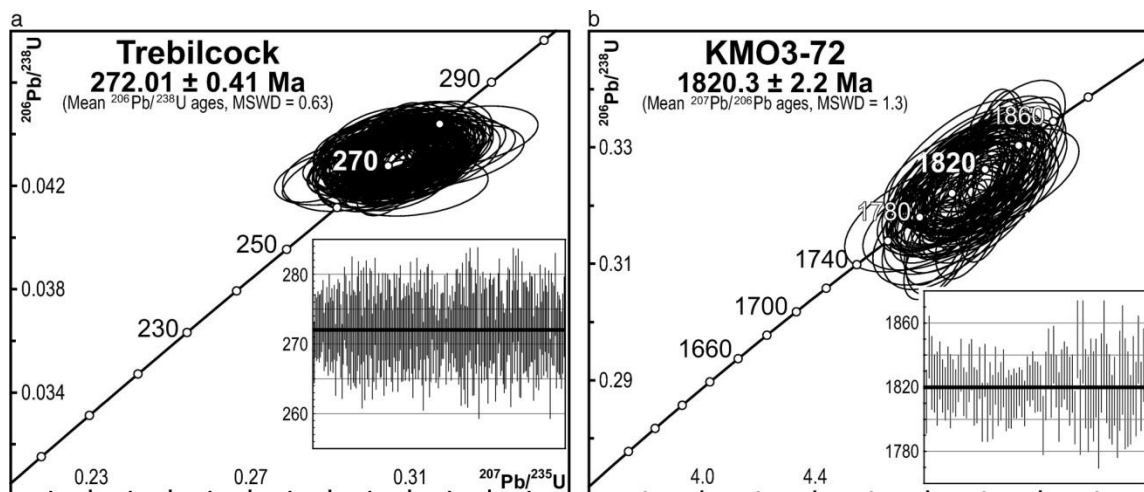


Fig. 7. Precision and accuracy of the U–Pb data collected on the two monazite standards used in this study: (a) the Trebilcock monazite that was used as the reference material; (b) the monazite KMO3-72 that was used as secondary standard.

Monazite KMO3-72 was analyzed 97 times. After discarding 13 outlier analyses (13%), a weighted average $^{207}\text{Pb}/^{206}\text{Pb}$ age was calculated at 1820.3 ± 2.2 Ma (MSWD = 1.3), agreeing with the TIMS age at 1822 ± 1.5 Ma (G. Dunning, unpublished data). Due to the relatively young age of Trebilcock monazite, potential bias (i.e., unreasonably large uncertainties) in the corrected $^{207}\text{Pb}/^{206}\text{Pb}$ ratios was expected for the unknown monazite samples. Analyzing the secondary standard KMO3-72 helped to monitor this bias. No significant difference was found between the (final) corrected and (initial) measured $^{207}\text{Pb}/^{206}\text{Pb}$ ratios for that older monazite, meaning that the measured $^{207}\text{Pb}/^{206}\text{Pb}$ ratios were accurate and did not need to be corrected when using Trebilcock. Therefore, these measured ratios and corresponding $^{207}\text{Pb}/^{206}\text{Pb}$ ages with their initial (smaller) uncertainties are the ones reported in that paper. Only the two U/Pb ratios were corrected for, and carry their propagated error. Based on the standard data, ages are accurate, and a precision of $\sim 2\%–3\%$ (2 SE (standard error)) was expected for our $^{207}\text{Pb}/^{206}\text{Pb}$ data. Common Pb corrections were not applied here.

Data rejection and presentation of the unknowns

For Grenvillian age monazite (i.e., broadly between ca. 1100 and 1000 Ma), a precision of $\sim 2\%–3\%$ translates into $\pm 20–30$ Ma for a single analysis; therefore, a significant overlap of the data are to be expected within this age range in the present study. Thus, only the highest quality analyses are considered here (Table 2; Fig. 8). The quality of an analysis was assessed by examining the following: (i) *the location of the U–Pb spot* as seen on a second set of BSE images acquired after analysis, on which we verified that our spots sampled the homogeneous area in the grain previously identified in BSE (these images are not shown here, as pits representing failed analyses would have significantly altered the clarity of the photos); (ii) *the precision on each isotopic age*, as data were eliminated if they showed large uncertainties that were clearly due to ablation anomalies; and (iii) *discordance*, which was calculated using the formula $[1 - (^{207}\text{Pb}/^{206}\text{Pb} \text{ age}) / (^{206}\text{Pb}/^{238}\text{U} \text{ age})]100$. Data points $>5\%$ discordant were rejected.

Table 2. Monazite U–Pb data for all four samples: 244, HJ60b, 216 (sections a, c), and 333x.

							Ratio				Ages								
An.	Mnz.	Spot	Grain area	BSE	Occur.		$^{207}\text{Pb}/^{235}\text{U}$		$^{206}\text{Pb}/^{238}\text{U}$		$^{207}\text{Pb}/^{206}\text{Pb}$		$^{207}\text{Pb}/^{235}\text{U}$		$^{206}\text{Pb}/^{238}\text{U}$		$^{207}\text{Pb}/^{206}\text{Pb}$		% disc.
							2 SE		2 SE		2 SE		2 SE		2 SE				
244 (UTM 522350 5724850)																			
b28	12	4	R	—	M		1.723	0.068	0.1725	0.0041	0.0727	0.0010	1017	26	1025	22	1006	28	2
i39	13	1	R	—	M		1.843	0.087	0.1798	0.0042	0.0731	0.0013	1062	29	1065	23	1017	36	5
b43	3	2	R	—	M		1.760	0.072	0.1749	0.0043	0.0732	0.0012	1032	26	1038	24	1019	33	2
i24	16	2	R	—	M		1.703	0.078	0.1720	0.0038	0.0733	0.0013	1011	29	1023	21	1022	36	0
i12	8	2	R	—	ad_Grt		1.735	0.082	0.1728	0.0039	0.0734	0.0013	1026	30	1027	22	1025	36	0
k03	13	2	R	—	M		1.869	0.088	0.1792	0.0042	0.0736	0.0013	1068	31	1063	23	1031	36	3
i38	14	3	R	—	M		1.832	0.085	0.1770	0.0043	0.0739	0.0012	1056	31	1050	23	1039	33	1
b44	3	3	R	—	M		1.771	0.071	0.1726	0.0041	0.0742	0.0011	1037	25	1026	23	1047	30	–2
k07	11	2	R	—	Grt		1.816	0.082	0.1743	0.0039	0.0745	0.0011	1050	30	1035	21	1055	30	–2
b34	9	2	R	—	M		1.822	0.074	0.1776	0.0042	0.0747	0.0013	1057	26	1054	23	1060	35	–1
b67	2	4	R	—	M		1.810	0.074	0.1779	0.0044	0.0747	0.0012	1045	27	1056	24	1060	32	0
i21	15	2	R	—	emb_Grt		1.780	0.084	0.1753	0.0041	0.0747	0.0012	1037	30	1041	22	1060	32	–2
b56	5	2	R	L	M		1.750	0.082	0.1737	0.0039	0.0748	0.0014	1028	31	1032	22	1063	38	–3
b40	4	2	R	—	M		1.857	0.078	0.1785	0.0045	0.0750	0.0015	1066	27	1059	24	1069	40	–1
b40	4	2	R	—	M		1.805	0.073	0.1740	0.0042	0.0752	0.0011	1045	26	1033	23	1074	29	–4
b53	1	4	R	—	Grt		1.900	0.074	0.1813	0.0045	0.0757	0.0009	1080	25	1074	25	1087	25	–1
b62	2	1	R	—	M		1.872	0.079	0.1776	0.0047	0.0764	0.0014	1066	27	1054	25	1106	37	–5
k09	11	3	R	—	Grt		2.135	0.098	0.1929	0.0043	0.0793	0.0011	1157	32	1136	23	1180	27	–4
b38	4	1	c	—	M		1.764	0.073	0.1744	0.0042	0.0729	0.0013	1031	27	1036	23	1011	36	2
i20	15	1	c	—	emb_Grt		1.797	0.084	0.1794	0.0042	0.0734	0.0014	1043	31	1064	23	1025	39	4
b22	17	1	c	—	M		1.757	0.072	0.1730	0.0041	0.0739	0.0013	1027	27	1029	22	1039	36	–1
b35	9	3	c	L	M		1.822	0.074	0.1784	0.0042	0.0739	0.0012	1051	26	1058	23	1039	33	2
i09	7	2	c	—	M		1.793	0.084	0.1743	0.0041	0.0741	0.0014	1041	30	1035	23	1044	38	–1
b65	2	3	c	—	M		1.770	0.073	0.1742	0.0042	0.0741	0.0012	1031	26	1035	23	1044	33	–1
i36	14	2	c	—	M		1.877	0.088	0.1788	0.0040	0.0744	0.0015	1072	31	1060	22	1052	41	1
b41	3	1	c	—	M		1.833	0.075	0.1783	0.0043	0.0745	0.0014	1054	27	1058	24	1055	38	0
b58	6	1	c	—	M		1.734	0.073	0.1700	0.0042	0.0745	0.0014	1022	26	1012	23	1055	38	–4
i11	8	1	c	—	ad_Grt		1.825	0.087	0.1773	0.0041	0.0748	0.0015	1054	31	1051	22	1063	40	–1
i23	16	1	c	—	M		1.763	0.082	0.1747	0.0038	0.0748	0.0013	1032	30	1037	21	1063	35	–3
b32	9	1	c	L	M		1.809	0.075	0.1760	0.0042	0.0749	0.0015	1049	27	1045	23	1066	40	–2
b64	2	2	c	—	M		1.805	0.078	0.1764	0.0045	0.0750	0.0015	1046	27	1047	25	1069	40	–2
i26	21	2	c	—	M		1.783	0.085	0.1764	0.0043	0.0750	0.0015	1039	31	1046	24	1069	40	–2
b26	12	3	c	—	M		1.879	0.076	0.1801	0.0045	0.0759	0.0013	1071	27	1067	24	1092	34	–2
i14	10	1	c	—	M		1.857	0.089	0.1769	0.0046	0.0764	0.0016	1067	32	1048	25	1106	42	–5
b47	1	1	c	—	Grt		2.144	0.084	0.1948	0.0048	0.0800	0.0009	1160	27	1146	26	1198	22	–5
k06	11	1	c	—	Grt		2.954	0.130	0.2353	0.0050	0.0898	0.0010	1395	35	1362	26	1421	21	–4
HJ60b (UTM 522750 5617620)																			
d42	6	2	R	—	M		1.730	0.066	0.1732	0.0049	0.0721	0.0010	1018	24	1029	27	988	28	4
f11	4	2	R	—	M		1.706	0.038	0.1676	0.0036	0.0738	0.0013	1009	14	999	20	1036	36	–4
f08	12	2	R	—	ad_Grt		1.830	0.040	0.1771	0.0039	0.0746	0.0013	1054	15	1051	21	1058	35	–1
d11	1	1	R	—	ad_Grt		1.872	0.067	0.1824	0.0050	0.0747	0.0009	1071	24	1081	27	1059	24	2
d33	8	3	R	—	M		1.866	0.068	0.1795	0.0049	0.0762	0.0010	1068	24	1064	27	1100	25	–3
d23	5	2	R	—	M		1.835	0.069	0.1794	0.0051	0.0761	0.0012	1057	25	1064	27	1098	32	–3
f09	4	1	c	—	M		1.863	0.041	0.1800	0.0042	0.0745	0.0013	1066	15	1065	23	1055	35	1
d22	5	1	c	—	M		1.929	0.077	0.1887	0.0057	0.0750	0.0014	1087	26	1114	31	1069	38	4
d40	6	1	c	—	M		1.862	0.073	0.1811	0.0053	0.0750	0.0014	1064	26	1072	29	1069	38	0
d12	1	2	c	—	ad_Grt		1.858	0.068	0.1796	0.0049	0.0753	0.0009	1067	24	1065	27	1076	25	–1
d39	11	2	c	—	ad_Grt		1.961	0.073	0.1876	0.0053	0.0755	0.0010	1101	25	1107	29	1081	26	2
d43	3	1	c	—	ad_Grt		1.912	0.070	0.1836	0.0051	0.0755	0.0009	1084	24	1087	28	1081	24	1
d34	11	1	c	—	ad_Grt		1.914	0.075	0.1852	0.0054	0.0755	0.0014	1085	25	1095	29	1082	37	1
d30	8	1	c	—	M		1.936	0.074	0.1852	0.0054	0.0769	0.0014	1090	26	1096	29	1119	36	–2
d31	8	2	c	—	M		2.494	0.092	0.2146	0.0058	0.0850	0.0011	1269	27	1252	31	1316	25	–5
f12	4	3	c	—	M		2.625	0.059	0.2230	0.0057	0.0855	0.0013	1302	17	1294	30	1327	29	–3
d26	9	1	c	—	M		3.297	0.120	0.2679	0.0080	0.0909	0.0013	1479	29	1527	40	1445	27	5
333x (UTM 518148 5643761)																			
c33	2	4	R	L	M		1.667	0.039	0.1694	0.0032	0.0718	0.0011	997	15	1008	18	980	31	3
c31	2	3	R	L	M		1.681	0.040	0.1696	0.0032	0.0723	0.0011	1001	15	1010	18	994	31	0
c36	11	1	R	L	M		1.721	0.040	0.1712	0.0031	0.0730	0.0011	1017	15	1019	17	1014	31	0
c19	1	2	R	L	Grt		1.910	0.049	0.1836	0.0035	0.0761	0.0015	1084	17	1085	19	1098	39	–1
c14	20	1	—	—	bi.cor_Grt		1.650	0.042	0.1665	0.0032	0.0719	0.0011	987	16	993	18	983	31	1
h23	6	1	c	d	M		1.735	0.087	0.1718	0.0044	0.0731	0.0016	1016	31	1022	24	1017	44	1
c11	35	2	—	—	M		1.778	0.048	0.1772	0.0035	0.0732	0.0014	1038	18	1051	19	1019	39	3
h20	15	2	c	d	ad_Grt		1.760	0.086	0.1744	0.0040	0.0740	0.0015	1027	31	1036	22	1041	41	–1
h09	16	1	c	—	ad_Grt		1.724	0.084	0.1714	0.0044	0.0740	0.0014	1012	31	1023	23	1041	38	–2
c44	3	2	c	d	M		1.799	0.038	0.1750	0.0031	0.0742	0.0008	1044	14	1040	17	1048	20	–1
c43	3	1	c	d	M		1.814	0.041	0.1770	0.0034	0.0743	0.0009	1049	15	1050	18	1051	25	0
h19	15	1	c	d	ad_Grt		1.807	0.087	0.1750	0.0039	0.0746	0.0014	1044	32	1039	21	1058	38	–2
c30	9	1	c	d	M		1.804	0.083	0.1747	0.0037	0.0749	0.0010	1046	30	1038	21	1064	26	–3
c30	9	1	c	d	M		1.861	0.040	0.1795	0.0033	0.0752	0.0008	1068	14	1064	18	1073	22	–1
c34	21	1	c	d	M		1.824	0.038	0.1757	0.003									

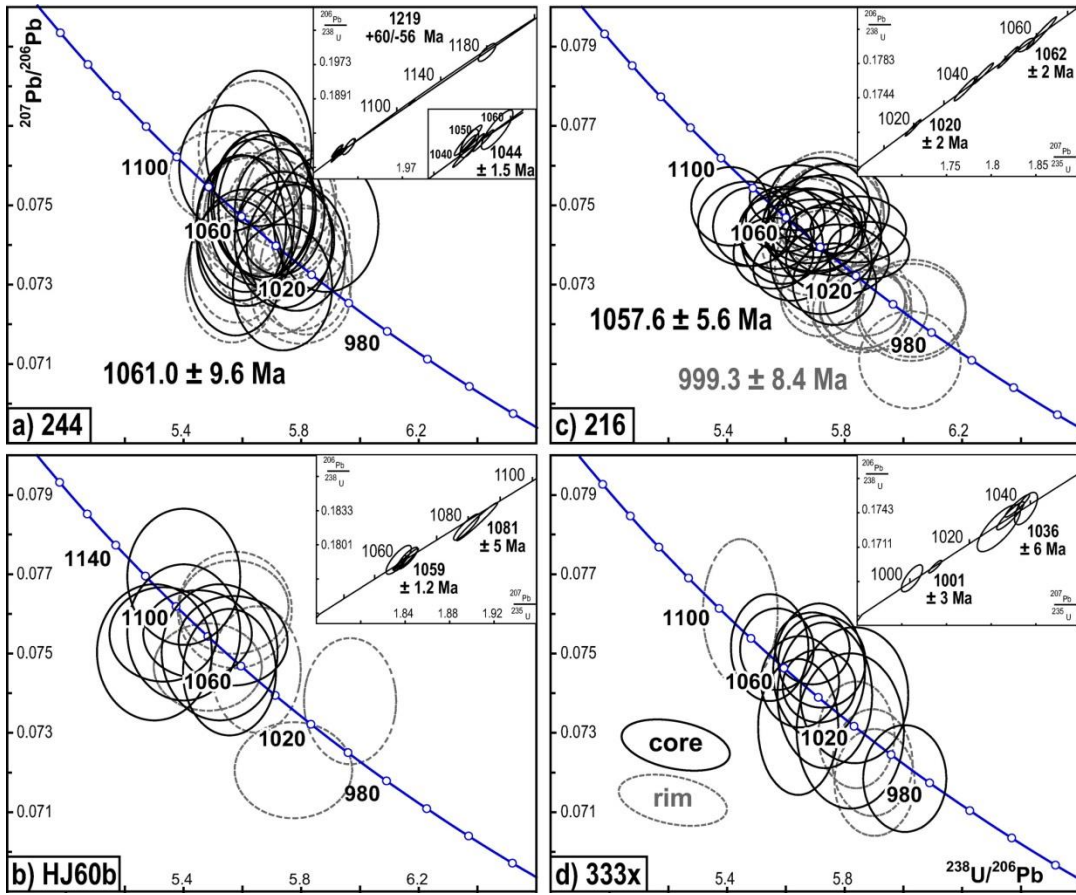


Fig. 8. Tera-Wasserburg diagrams presenting the U–Pb data collected for each sample, with inset showing the corresponding ID–TIMS data modified after Dunning and Indares (2010): (a) sample 244; (b) sample HJ60b; (c) sample 216; (d) sample 333x.

After data assessment, 106 U–Pb analyses collected on 64 grains were kept (Table 2). Ages cited are $^{207}\text{Pb}/^{206}\text{Pb}$ unless stated otherwise. Grains that produced the most significant ages (e.g., the oldest or youngest age in a sample, or distinct ages in core and rim) and also served as example of the various types of internal zoning are shown in Fig. 5, with the location of the 20 μm laser ablation pits and corresponding $^{207}\text{Pb}/^{206}\text{Pb}$ age.

Results

Datasets vary in size from 16 U–Pb analyses carried out on 11 monazite grains in sample 333x to 37 analyses done on 26 grains in sample 216 (including grains in both samples 216a and 216c; Table 2). The main population of data points is between ca. 1100 and 1000 Ma in all samples (Fig. 8), with a general trend of BSE-dark cores yielding older ages than BSE-light rims (Fig. 8). Older ages between 1500 and 1150 Ma are only found in samples HJ60b and 244 and are recorded in monazite grains included in garnet and (or) cores of matrix grains (Table 2). The main data population falls within the range of the Grenvillian orogeny and will be referred to in the text as “Grenvillian”, while the older data points will be referred to as “pre-Grenvillian”.

Pre-Grenvillian ages

Six analyses in samples 244 and HJ60b yielded distinctively pre-Grenvillian ages (Table 2; Fig. 8). In sample 244, these are 1421 ± 21 , 1180 ± 27 , and 1198 ± 22 Ma and were retrieved in cores and (or) rim of monazite grains 1 and 11 included in garnet (Fig. 5b). In contrast, in sample HJ60b, the oldest ages, at 1445 ± 27 Ma (core of grain 9), 1327 ± 23 Ma (grain 4) and 1316 ± 25 Ma (core of grain 8; Fig. 5b) are recorded by matrix monazite.

Grenvillian ages

The predominant monazite ages in all samples are Grenvillian (Table 2; Fig. 8), in the general range between 1119 and 960 Ma, with the largest concentration within the interval 1069–1050 Ma.

In sample 244, monazite ages are between 1106 ± 42 Ma (core of matrix grain 10) and 1006 ± 28 Ma (BSE-light rim of matrix grain 12) and cluster at 1050–1070 Ma, with 14 analyses giving a weighted average $^{207}\text{Pb}/^{206}\text{Pb}$ age of 1061 ± 9.6 Ma (MSWD = 0.081; Table 2; Figs. 5a, 8a). Most of the data in this interval come from matrix grains, except for rims of grains 11 and 24, which are included in garnet. In addition, a few grains show clear age differences between core and rim; for instance, 1092 ± 34 Ma versus 1006 ± 28 Ma in grain 12 (Fig. 5a).

The majority of monazite ages in sample HJ60b (Fig. 8b) are between 1055 ± 35 and 1082 ± 37 Ma (cores of grains 4 and 11; Table 2; Fig. 5b). A few older ages (1100 ± 25 , 1098 ± 32 , and 1119 ± 36 Ma) come from grains with pre-Grenvillian cores (e.g., grain 8, Fig. 5b). In addition, a distinctively younger age at 988 ± 28 Ma is recorded at the rim of grain 6, the core of which yielded an age at 1069 ± 38 Ma (Fig. 5b). This grain is included in a thin quartz film around garnet.

In sample 216 (Figs. 8c), monazite data mainly range between 1074 ± 18 and 994 ± 28 Ma, with two clusters for which weighted average $^{207}\text{Pb}/^{206}\text{Pb}$ ages were calculated at 1057.6 ± 5.6 Ma ($n = 16$, MSWD = 0.32) and 999.3 ± 8.4 Ma ($n = 8$, MSWD = 0.119). The oldest ages are recorded in BSE-dark cores of monazite, and the youngest ones in distinctive BSE-bright rims, common in matrix grains (Table 2). Several analyzed grains show age differences of over 50 million years between the older core and the younger rim (Figs. 5c, 5d).

In sample 333x, monazite the oldest age (1098 ± 39 Ma) was recorded by the thick BSE-light rim of grain 1 included in garnet (Fig. 5e). Other ages mostly range between 1074 ± 29 and 1041 ± 38 Ma (mostly BSE-dark cores of matrix grains or grains adjacent to garnet) without any particular cluster (Fig. 8d). In addition, a set of distinctly younger ages (1014 ± 31 to 980 ± 31 Ma) is recorded in BSE-bright rims (e.g., grain 2; Fig. 5e; and grain 20 included in texturally late biotite corroding garnet).

Discussion

Monazite textures

In granulite-facies aluminous rocks, monazite included in garnet is expected to record ages of prograde metamorphism or previous metamorphic events (if any), whereas matrix monazite, in addition, may also record the age range of melt crystallization as well as later fluid infiltration, if applicable. Indeed for matrix monazite in sample 216c (Figs. 3, 5), individual grains often show complex internal zoning where the distinction between a core and one or more rims is not clear. This is because the two-dimensional images may not always properly reflect the three-dimensional geometry in which the different monazite growth domains of different compositions and (or) U–Pb ages may be actually organized (cf., Spear and Pyle 2002). However, even in two-dimensional, the complex internal textures of several grains are clearly consistent with overgrowths on corroded earlier monazite (e.g., grain 20 in sample 216c). Because of the anatectic nature of the host rocks, such features might be explained by partial dissolution of earlier monazite in the melt followed by new growth during melt crystallization or a later fluid infiltration event.

In situ LA–ICP–MS dating of monazite revealed three distinct sets of ages in the aluminous gneisses of the PLV and the LBS. These data are complementary to the ID–TIMS data on monazite ([Dunning and Indares 2010](#)) and LA–ICP–MS data on metamorphic zircon from the same samples ([Lasalle et al. 2013](#)) and place further constraints on the thermal evolution of these rocks.

Age data

Pre-Grenvillian ages

Pre-Grenvillian ages were exclusively found in rocks inferred to have originated as sedimentary layers: sample HJ60b from the mid-*P* PLV, and sample 244 from the northern extension of the LBS into the high-*P* segment. The oldest age (ca. 1445 Ma) was recorded by sample HJ60b from the PLV, and is close to the inferred deposition age of this sequence ([Lasalle et al. 2013](#); [Moukhsil et al. 2013](#)). In sample 244, from the inferred extension of the LBS in the Manicouagan Imbricate Zone, the oldest monazite (ca. 1421 Ma) predates the ca. 1238 Ma age of formation of the LBS, as determined in the Canyon domain ([Lasalle et al. 2013](#)), and implies the presence of an older crustal component in this northern part of the sequence.

Grenvillian age metamorphism

The data revealed two groups of Grenvillian ages. The oldest and predominant group, qualified as “main” Grenvillian, was recorded in grains and portions of grains relatively dark in BSE, and the youngest, “late” Grenvillian, in distinctive BSE-bright rims of matrix monazite.

Main Grenvillian ages cover a variably wide range in individual samples, with a main concentration between ca. 1070 and 1050 Ma. In addition, samples HJ60b and 244 show some older ages (e.g., 1087 Ma in sample 244, and 1081–1082 Ma in sample HJ60b), and samples 244, 331x, and 216 show a trail of younger ages down to ca. 1025 Ma (more evenly distributed in the case of sample 333x). The questions here are as follows: (i) At which time within this range did the predominant granulite-facies mineral assemblage developed in these rocks?; (ii) What is the meaning of the age spread? These can be addressed by considering a simplified scenario of monazite growth/consumption in anatectic rocks (Fig. 9, showing the P – T path of sample HJ60b). The rationale is that monazite can grow during prograde metamorphism, up to the onset of partial melting (M_{gr} (P) in Fig. 9). Once melting begins, prograde or earlier monazite would tend to dissolve in the melt, and then new monazite growth would occur during melt loss or subsequent melt crystallization (M_{gr} (R) in Fig. 9; see Kelsey et al. 2008). Therefore, ideally, the age of the peak can be bracketed between the last growth of prograde monazite and the first growth by melt crystallization (retrograde). Prograde monazite can be preserved anywhere in a rock (and preferentially as inclusions in garnet, where it is protected from later dissolution), whereas retrograde monazite would be restricted to the matrix.

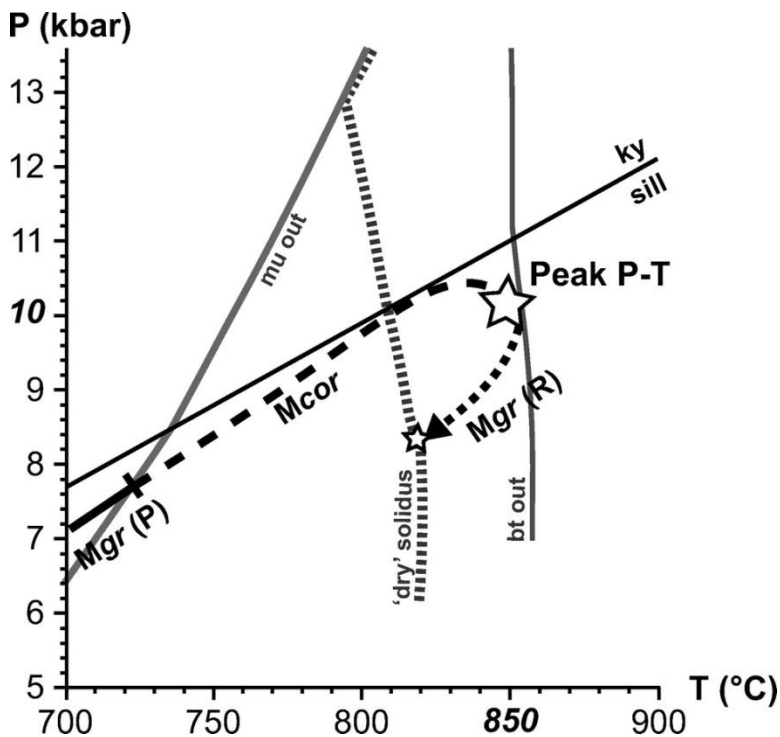


Fig. 9. Schematic P – T path modelled for the mid- P sample HJ60b (inspired by Lasalle and Indares 2014) showing presumed P – T ranges of monazite growth (M_{gr}), with a distinction between prograde (P) and retrograde (R), and the P – T range of monazite corrosion (M_{cor}). Important boundaries copied from the pseudosections (presented in Lasalle and Indares 2014) are also reported. mu-out line: reaction muscovite + quartz \pm plagioclase \rightarrow Al-silicate + K-feldspar + liquid; between the mu-out line and the bt-out line: continuous partial melting by reaction: biotite + Al-silicate + quartz \pm plagioclase \rightarrow garnet + K-feldspar + liquid; “dry” solidus: position of the solidus after melt loss. 1 kbar = 100 MPa.

Although some monazite grains in garnet record the oldest (or among the oldest) Grenvillian ages (e.g., grain 1, sample 333x; grain 1, sample HJ60b), in other instances they show ages on the younger side of the main clusters (e.g., 1050–1055 Ma: rims of grains 24 and 11 in sample 244; 1059 Ma: rim of grain 1 in sample HJ60b; and 1048 Ma: core of grain 17 in sample 216c). This may mean that the main cluster of data represents ages close to the granulite-facies metamorphic peak, and differences between the last prograde monazite growth and that at early stages of melt crystallization are not resolvable with the resolution of data in this study (± 20 –40 Ma). However, the general trend of data trailing down to ca. 1025 Ma (samples 333x, 216, 244) would be consistent with protracted post thermal peak growth of monazite over several tens of million years.

Late Grenvillian ages between ca. 1014 and ca. 980 Ma were recorded in monazite from all four samples, most commonly in sample 216 (Table 2; Fig. 8). In contrast to the previous sets of ages, these come from distinctive textural zones, the BSE-bright and Th-enriched rims of various widths that are common in many matrix grains, and are inferred to represent a distinct monazite growth event.

In some instances, the young BSE-bright domains clearly overgrow corroded earlier monazite as in the case of grain 20 in sample 216c (Fig. 5d), the internal texture of which shows a complex succession of at least three distinct episodes of growth – corrosion – new growth. The central part of the grain, as well as its thick rim, even displays a compositional gradation in Th content. We attribute the earlier episodes of corrosion – new growth to dissolution of monazite in anatectic melt and regrowth during melt crystallization. In contrast, we interpret the late growth of the BSE-light rims to be related to an influx of fluids, which is consistent with, and likely coeval to, the chlorite-filled cracks in garnet and pseudomorph of the sillimanite by very fine aggregates, possibly sericite, in samples 216 and HJ60b (Fig. 3).

Comparison with the ID–TIMS data

Monazite ID–TIMS data from Dunning and Indares (2010) are shown as inset in Fig. 8. Due to the different scale of precision between those (± 2 million years) and our LA–ICP–MS data (± 20 –40 million years; main plots Fig. 8), we cannot directly compare them. However, a few inferences can be drawn concerning the main Grenvillian ages: (i) in samples 244 and 331x, the new data show a predominance of older ages relative to the TIMS data (ca. 1060 Ma versus 1040 Ma); and (ii) for samples HJ60b and 216, the age ranges are broadly similar. Most importantly, the late Grenvillian event which is clearly documented here was missed by the ID–TIMS study (except for a 1001 ± 3 Ma age reported in 333x by Dunning and Indares 2010). A likely explanation is that the abrasion process (Krogh 1982) used to clean up grains before isotopic dilution TIMS analysis eliminated the thin monazite rims that were targeted in this LA–ICP–MS study. However, as shown on the BSE images, rims with such a young age can, in rare cases, be relatively wide (e.g., BSE-light rim in grain 2, sample 333x, Fig. 5e), and these would not be completely removed by abrasion, which in turn would explain some mixed ages produced by TIMS.

Regional implications

The main Grenvillian age ranges reported here do not show any major difference between samples belonging to the high-*P* (sample 244) and mid-*P* segments of the hinterland (samples HJ60b, 216a, 216c, and 331x). However, the wide age ranges reported here as well as in Dunning and Indares (2010) contrast with the very restricted ages reported from the eastern portion of the high-*P* segment in the same area (Fig. 1; Indares and Dunning 2001) and imply that the duration of the main Grenvillian metamorphism in this segment was variable. We finally note that the main Grenvillian age ranges determined in this study are also similar to those reported from other granulite-facies portions of the Grenvillian hinterland (see in Rivers 2008).

In contrast, this is the first report of late Grenvillian metamorphism in the hinterland. This event is attributed to infiltration of hot fluids under (sub-) greenschist-facies conditions and is coeval with the following: (i) widespread intrusion of pegmatites and ultrapotassic dykes at 980–990 Ma in the Canyon domain (Dunning and Indares 2010; Valverde Cardenas et al. 2012); and (ii) high-*P* granulite-facies metamorphism on the parautochthonous footwall of the hinterland (Jordan et al. 2006). These features represent a major change in the orogenic evolution, which is attributed by Rivers (2012) to orogenic collapse.

Conclusions

In situ LA–ICP–MS dating of monazite in granulite-facies anatectic aluminous gneisses provides new constraints on the thermal evolution of the central part of the Grenvillian hinterland.

Monazite ages are linked to physical characteristics of the dated grains, with BSE-dark cores (or entire grains) giving consistently older ages than BSE-bright rims. The BSE-dark monazite gave a wide range of ages, some of which are inherited from earlier events and are only recorded in the metasedimentary samples (HJ60b and 244). The range of the main Grenvillian ages (~1070–1020 Ma) is comparable to that of the data of Dunning and Indares (2010), some of which were questioned as potentially representing mixed ages. However, the present study shows that the spread is real. In the context of the granulite-facies anatectic host rocks, this spread of monazite ages may represent distinct monazite growth episodes linked to melt crystallization pulses in crustal rocks that remained under high-*T* conditions for a protracted period of time.

In contrast, the distinctly younger (ca. 1010–990 Ma) BSE-light rims are attributed to fluid circulation, under greenschist metamorphic conditions, linked to the intrusion of ultrapotassic dykes and felsic pegmatite in the Canyon domain. This event is coeval with high-grade metamorphism in the underlying Parautochthonous belt, and the final propagation of the orogen to the northwest, and therefore it likely records the response of the hinterland to orogenic collapse.

Acknowledgements

Samples were collected in 2004 by A. Indares, and this research is part of the Ph.D. project of the first author. We thank several people from the MicroAnalysis facility (MAF-IIC labs) at the Bruneau Center (Memorial University) for their help and support during our work: M. Tubrett, Dr. R. Lam, and W. Diegor

from the LA–ICP–MS lab, and M. Shaffer and Dr. D. Grant from the SEM–CL lab. We also thank R. Jamieson for providing access to the EPMA laboratory at Dalhousie University. The detailed, helpful, and very clear comments from Chris McFarlane (Associate Editor), Fernando Corfu, and one anonymous reviewer are gratefully acknowledged. Ali Polat is thanked for editorial handling. This work was supported by a Natural Sciences and Engineering Research Council of Canada (NSERC) Discovery grant to A. Indares.

References

- Beaumont, C., Nguyen, M.H., Jamieson, R.A., and Ellis, S. 2006. Crustal flow modes in large hot orogens. *In* Channel flow, ductile extrusion and exhumation in continental collision zones. *Edited by* R.D. Law, M.P. Searle, and L. Godin. Geological Society (of London), Special Publication 268. pp. 91–145
- Brown M. 2004. The mechanism of melt extraction from lower continental crust of orogens. *Transactions of the Royal Society of Edinburgh, Earth Sciences* **95**: 35–48
- Cherniak DJ, Watson EB, Grove M, Harrison TM. 2004. Pb diffusion in monazite: a combined RBS/SIMS study. *Geochimica et Cosmochimica Acta* **68**: 829–840
- Cox RA, Dunning GR, Indares A. 1998. Petrology and U–Pb geochronology of mafic, high-pressure metamorphic coronites from the Tshenukutish domain, eastern Grenville Province. *Precambrian Research* **90**: 59–83
- Cutts KA, Kinny PD, Strachan RA, Hand M, Kelsey DE, Emery M, Friend CRL, Leslie AG. 2010. Three metamorphic events recorded in a single garnet: Integrated phase modelling, in situ LA–ICPMS and SIMS geochronology from the Moine Supergroup, NW Scotland. *Journal of Metamorphic Geology* **28**: 249–267
- Dunning G, Indares A. 2010. New insights on the 1.7–1.0 Ga crustal evolution of the central Grenville Province from the Manicouagan – Baie Comeau transect. *Precambrian Research* **180**: 204–226
- Fisher CM, McFarlane CRM, Hanchar JM, Schmitz MD, Sylvester PJ, Lam R, Longerich HP. 2011. Sm–Nd isotope systematics by laser ablation-multicollector-inductively coupled plasma mass spectrometry: Methods and potential natural and synthetic reference materials. *Chemical Geology* **284**: 1–20
- Gervais F, Hynes A. 2012. Linking metamorphic textures to U–Pb monazite in-situ geochronology to determine the age and nature of aluminosilicate-forming reactions in the Northern Monashee Mountains, British-Columbia. *Lithos* **160–161**: 250–267
- Gower CF, Krogh TE. 2002. A U–Pb geochronological review of the Proterozoic history of the eastern Grenville Province. *Canadian Journal of Earth Sciences* **39** (5): 795–829
- Harrison, T.M., Catlos, E.J., and Montel, J.-M. 2002. U–Th–Pb dating of phosphate minerals. *In* Phosphates: geochemical, geobiological, and materials importance. *Edited by* M.J. Kohn, J. Rakovan, and J.M. Hughes. *Reviews in Mineralogy and Geochemistry*, 48(14). Mineralogical Society of America, pp. 523–558
- Hindemith, M.A. 2014. Petrography and geochemistry of hydrothermally altered volcanic rocks metamorphosed at granulite-facies conditions: and example from the Central Grenville Province. Msc Thesis, Earth Sciences Department, Memorial University of Newfoundland, St John's
- Indares A, Dunning G. 2001. Partial melting of high P–T metapelites from the Tshenukutish terrane (Grenville Province): petrography and U–Pb geochronology. *Journal of Petrology* **42**: 1547–1565
- Indares A, Dunning G. 2004. Crustal architecture above the high-pressure belt of the Grenville Province in the Manicouagan area: new structural, petrologic and U–Pb age constraints. *Precambrian Research* **130**: 199–208

- Indares A, Moukhsil A. 2013. Geon 12 crustal extension in the central Grenville Province, implications for the orogenic architecture, and potential influence on the emplacement of anorthosites. *Canadian Journal of Earth Sciences* **50**(9): 955-966
- Indares A, Dunning G, Cox R. 2000. Tectono-thermal evolution of deep crust in a Meso-proterozoic continental collision setting: the Manicouagan example. *Canadian Journal of Earth Sciences* **37**(2–3): 325-340
- Jamieson RA, Beaumont C. 2011. Coeval thrusting and extension during lower crustal ductile flow – implications for exhumation of high grade metamorphic rocks. *Journal of Metamorphic Geology* **29**: 33-51
- Jamieson RA, Beaumont C, Nguyen MH, Culshaw NG. 2007. Syn-convergent ductile flow in variable strength continental crust: Numerical models with applications to the western Grenville orogen. *Tectonics* **26**: 1-23
- Jamieson RA, Beaumont CJ, Warren CJ, Nguyen MH. 2010. The Grenville orogen explained? Applications and limitations in integrating numerical models with geological and geophysical data. *Canadian Journal of Earth Sciences* **47** (4): 517-539
- Jordan SL, Indares A, Dunning G. 2006. Partial melting of metapelites in the Gagnon terrane below the high-pressure belt in the Manicouagan area (Grenville Province): pressure-temperature (P-T) and U-Pb age constraints and implications. *Canadian Journal of Earth Sciences* **43** (9): 1309-1329 Link, ISI, Abstract
- Kelly NM, Harley SL, Möller A. 2012. Complexity in the behavior and recrystallization of monazite during high-T metamorphism and fluid infiltration. *Chemical geology* **322–323**: 192-208
- Kelsey DE, Hand M, Clark C, Wilson CJL. 2007. On the application of in situ monazite chemical geochronology to constraining P-T-t histories in high-temperature (>850 °C) polymetamorphic granulites from Prydz Bay, East Antarctica. *Journal of the Geological Society* **164**: 667-683
- Kelsey DE, Clark C, Hand M. 2008. Thermobarometric modelling of zircon and monazite growth in melt-bearing systems: examples using model metapelitic and metapsammitic granulites. *Journal of Metamorphic Geology* **26**: 199-212
- Krogh TE. 1982. Improved accuracy of U-Pb zircon ages by the creation of more concordant systems using an air abrasion technique. *Geochimica et Cosmochimica Acta* **46**: 637-649
- Langone A, Braga R, Massonne HJ, Tiepolo M. 2011. Preservation of old (prograde metamorphic) U–Th–Pb ages in unshielded monazite from the high-pressure paragneisses of the Variscan Ulten Zone (Italy) *Lithos* **127**: 68-85
- Lasalle S, Indares A. 2014. Anatectic record and contrasting *P–T* paths of aluminous gneisses from the central Grenville Province. *Journal of Metamorphic Geology*. In press
- Lasalle S, Fisher CM, Indares A, Dunning G. 2013. Contrasting types of Grenvillian granulite facies aluminous gneisses: Insights on protoliths and metamorphic events from zircon morphologies and ages. *Precambrian Research* **228**: 117-130
- Ludwig, K.R. 2003. User's manual for Isoplot/Ex, Version 3.0. A geochronological toolkit for Microsoft Excel: Berkeley Geochronology Center Special Publication, 4: 70 p
- Moukhsil, A., Solgadi, F., Lacoste, P., Gagnon, M., and David, J. 2012. Géologie de la région du lac du Milieu (SNRC 22O03, 22O04, 22O06, 22J13 et 22J14). Ministère des Ressources naturelles et de la Faune, RG 2012–01
- Moukhsil, A., Solgadi, F., Clark, T., Indares, A., and Blouin, S. 2013. Geology of the Daniel-Johnson Dam (Manic 5) area, Côte-Nord region (NTS 22K14, 22K15, 22K16, 22N03 and 22N02). Ministère des Ressources naturelles et de la Faune, RG-2013

- Owens BE, Tomascak PB. 2002. Mesoproterozoic lamprophyres in the Labrieville Massif, Quebec: clues to the origin of alkalic anorthosites? *Canadian Journal of Earth Sciences* **39** (6): 983-997
- Paton C, Woodhead J, Hellstrom J, Hergt J, Greig A, Maas R. 2010. Improved laser ablation U–Pb zircon geochronology through robust downhole fractionation correction. *Geochemistry Geophysics Geosystems* **11**: 1-36
- Rivers T. 2008. Assembly and preservation of lower, mid, and upper orogenic crust in the Grenville Province- Implications for the evolution of large hot long-duration orogens. *Precambrian Research* **167**: 237-259
- Rivers, T. 2009. The Grenville Province as a large hot long-duration collisional orogen — insights from the spatial and thermal evolution of its orogenic fronts. *In* *Ancient orogens and modern analogues. Edited by J.B. Murphy, J.D. Keppie, and A. Hynes. Geological Society (of London), Special Publication 327. pp. 405–444. 10.1144/SP327.17*
- Rivers T. 2012. Upper-crustal orogenic lid and mid-crustal core complexes: signature of a collapsed orogenic plateau in the hinterland of the Grenville Province. *Canadian Journal of Earth Sciences* **49**(1): 1-42
- Rivers T, Martignole J, Gower CF, Davidson A. 1989. New tectonic divisions of the Grenville province, southeast Canadian Shield. *Tectonics* **8**: 63-84
- Rivers, T., Culshaw, N., Hynes, A., Indares, A., Jamieson, R., and Martignole, J. 2012. The Grenville Orogen - A post-LITHOPROBE perspective. *In* *Tectonic Styles in Canada: The LITHOPROBE Perspective. Chapter 3. Edited by J.A. Percival, F.A. Cook, and R.M. Clowes. Geological Association of Canada, Special Paper 49, pp. 97–236*
- Shaffer, M. 2009. Discrimination of hematite and magnetite and quantifying their associations using the JKTECH Mineral Liberation Analyzer™. *In* *The 48th Annual Conference of Metallurgists, Laurentian University, Sudbury, Ontario 73*
- Shaffer, M., Gu, Y., and Rohde, M. 2008. Practical Applications for the Silicon Drift Xray Detector in SEM-Platformed Image Analysis: The Bruker-MLA in Practice. *In* *SME Annual Meeting 2007 and CMS 109th National Western Conference 2007 The Power of Mining: Energy's Influence, Denver, CO, U.S.A., 25–28 February 2007, 1(Preprint 07-029). pp. 1–6*
- Simonetti A, Heaman LM, Chacko T, Banerjee NR. 2006. In situ petrographic thin section U–Pb dating of zircon, monazite and titanite using laser ablation-MC-ICP-MS, *International Journal of Mass Spectrometry* **253**: 87-97
- Slagstad T, Hamilton MA, Jamieson RA, Culshaw NG. 2004. Timing and duration of melting in the mid orogenic crust: constraints from U-Pb (SHRIMP) data, Muskoka and Shawanaga domains, Grenville Province, Ontario. *Canadian Journal of Earth Sciences* **41** (11): 1339-1365
- Spear, F.S., Pyle, J.M. 2002. Apatite, Monazite, and Xenotime in Metamorphic Rocks. *In* *Phosphates: geochemical, geobiological, and materials importance. Edited by M.J. Kohn, J. Rakovan, and J.M. Hughes. Reviews in Mineralogy and Geochemistry, Vol. 48(7). Mineralogical Society of America, pp. 293–336.*
- Spear FS, Pyle JM. 2010. Theoretical modeling of monazite growth in a low-Ca metapelite. *Chemical Geology* **273**: 111-119
- Tomascak PB, Krogstad EJ, Walker RJ. 1996. U–Pb monazite geochronology of granitic rocks from Maine: Implications for Late Paleozoic tectonics in the northern Appalachians. *Journal of Geology* **104**: 185-195

- Valver de Cardenas C, Indares A, Jenner G. 2012. Mafic and ultrapotassic rocks from the Canyon domain (central Grenville Province): geochemistry and tectonic implications. *Canadian Journal of Earth Sciences* **49** (2): 412-433
- van Gool, J.A.M., Rivers, T., and Calon, T. 2008. Grenville Front zone, Gagnon terrane, south-western Labrador: configuration of a midcrustal foreland fold-thrust belt. *Tectonics*, **27**, TC1004,10.1029/20067C002095. WaveMetrics, Inc. IGOR Pro 6.3 manual, Lake Oswego, OR, www.wavemetrics.com
- Williams ML, Jercinovic MJ, Hetherington CJ. 2007. Microprobe monazite geochronology: Understanding geologic processes by integrating composition and chronology. *Annual Review Earth Planetary Sciences* **35**: 137-175